Experimental validation of large-scale simulations of dynamic fracture along weak planes

Vijaya B. Chalivendra [a,*], Soonsung Hong [b], Irene Arias [c], Jaroslaw Knap [d], Ares Rosakis [e], Michael Ortiz [e]

[a] Department of Mechanical Engineering, University of Massachusetts, North Dartmouth, MA 02427, USA
[b] Department of Mechanical Engineering, Michigan State University, East Lansing, MI 48824, USA
[c] Dep. de Matemàtica Aplicada III, Universitat Politècnica de Catalunya, Barcelona 08034, Spain
[d] Lawrence Livermore National Laboratory, Livermore, CA 94450, USA
[e] Graduate Aeronautical Laboratories, California Institute of Technology, CA 91125, USA

ARTICLE INFO

ABSTRACT

A well-controlled and minimal experimental scheme for dynamic fracture along weak planes is specifically designed for the validation of large-scale simulations using cohesive finite elements. The role of the experiments in the integrated approach is two-fold. On the one hand, careful measurements provide accurate boundary conditions and material parameters for a complete setup of the simulations without free parameters. On the other hand, quantitative performance metrics are provided by the experiments, which are compared *a posteriori* with the results of the simulations. A modified Hopkinson bar setup in association with notch-face loading is used to obtain controlled loading of the fracture specimens. An inverse problem of cohesive zone modeling is performed to obtain accurate mode-I cohesive zone laws from experimentally measured deformation fields. The speckle interferometry technique is employed to obtain the experimentally measured deformation field. Dynamic photoelasticity in conjunction with high-speed photography is used to capture experimental records of crack propagation. The comparison shows that both the experiments and the numerical simulations result in very similar crack initiation times and produce crack tip velocities which differ by less than 6%. The results also confirm that the detailed shape of the non-linear cohesive zone law has no significant influence on the numerical results.

© 2008 Elsevier Ltd. All rights reserved.

1. Introduction

Both theoretical and experimental studies on crack propagation in brittle materials under dynamic opening loading conditions have been extensively reported for the past 50 years [1–3]. A complete understanding of the opening-mode crack initiation and the subsequent crack growth phenomenon both in monolithic homogeneous brittle solids and along weak interfaces between homogeneous solids has also been reported by several authors in the past five decades [4–9]. Although dynamic fracture is to some extent well understood, predictive simulations remain a challenge. Indeed, the actual predictive power of dynamic fracture simulations is hindered by huge computational requirements for resolved models, along with modeling uncertainties regarding the boundary conditions and the fracture parameters.

Researchers have resorted to various kinds of validation methodologies for dynamic fracture simulations [10–12]. In most

studies, the numerical simulations are performed based on inputs taken from published experimental data. These inputs are often insufficient to completely setup a simulation, which therefore leaves room for the fitting of parameters. Then, the results of these simulations are validated against those of experiments published in the literature. These attempts highlight the need for integrated experiment-simulation approaches. Hao et al. [10] validated simulations of intersonic crack growth along weak planes under asymmetric dynamic loading, which was experimentally observed by Rosakis et al. [13] and Rosakis [3]. In their simulations, the input loading conditions were inferred from the projectile impact speeds published in the experimental work. Due to the contact processes, the projectile impact speed is insufficient to completely determine the actual loading on the specimen. Kandula et al. [14] validated their dynamic fracture simulations on functionally graded materials using the experiments performed by Parameswaran and Shukla [15]. In their simulations, specimen loading was approximated with point loads at a distance behind the crack tip and validated crack tip position results to those of experiments done by Parameswaran and Shukla [15] and Evora et al. [16]. The premise of the present work, also implemented by other researchers in related

---

* Corresponding author.
E-mail address: vchalivendra@umassd.edu (V.B. Chalivendra).

topics, is that the development of a successful verification and validation (V and V) program requires close collaboration between the experimentalist and the numerical analyst.

In addition to loading conditions, there are uncertainties in the cohesive properties of the material, here an interface. The current opinion in the field of cohesive zone modeling of fracture is that the cohesive zone law can be described by two independent parameters out of the following three parameters: cohesive energy, cohesive strength and the separation length. In most of the cases, the first two parameters are obtained from the global standard experimental measurements for a given material. For instance, Mohammed and Liechti [17] employed global measurements of intrinsic interfacial toughness, maximum traction or stress and initial slope in the cohesive zone model proposed by Needleman [18,19] to perform simulations of crack nucleation at bi-material interfaces. Recently, Bjerke and Lambros [20] formulated cohesive-opening laws for simulations of dynamic fracture of brittle PMMA under impact loading on the basis of dynamic energy rate measurements by the strain gage technique and tensile strength measured in uniaxial tensile tests. The global measurements inaccurately represent the crack tip process zone because they involve several uncertain variables. These uncertainties demand a separate experimental investigation to extract accurate cohesive zone laws from the experimentally measured deformation field around the crack tip.

Motivated by the limitations of previous validation studies and the need for more systematic validation methods, we report here a coordinated effort to validate experimentally large-scale finite element simulations of dynamic fracture using cohesive zone models. The outline of the article is as follows. In Section 2, the experimental design considerations and procedures to provide valid inputs to numerical simulations are discussed. The performance metrics and their measurement are also given. In Section 3, the numerical design considerations are discussed. In Section 4, results of experiments are discussed and the validation of numerical results with experimental metrics is also discussed. Section 5 collects the conclusions of the study.

2. Experimental design considerations

The experimental design considerations focus on three main aspects. These are (1) designing a minimal dynamic fracture experiment which retains the essential phenomena under investigation, (2) designing an experimental setup to provide accurate boundary conditions, and finally (3) designing independent experiments to provide realistic cohesive zone laws. The details of all three aspects are discussed in the subsections below.

2.1. Design considerations in dynamic fracture experiments

The requirements of the numerical calculations and the search for the simplest setup that probes dynamic fracture guide the design of the experiments. In particular, to isolate fracture phenomena from the bulk constitutive material response, brittle materials are considered. At this stage, interfacial fracture is considered to avoid complex fracture processes such as crack branching. The size of the sample is also important, in that it needs to be large enough to delay the interference of the reflected waves with the crack tip, but not too large to keep the computational cost manageable. Finally, the quantitative comparative study requires high resolution full-field diagnostics, including dynamic crack propagation histories.

With this in mind, a brittle polyester based polymer, Homalite-100 is used as a specimen material. The main reasons for choosing Homalite-100 are (a) its bulk constitutive behavior can be well approximated by elasticity and (b) its properties are well documented in the literature. Some of the physical properties of Homalite-100 are listed in Table 1. A simple specimen configuration as shown in Fig. 1 is chosen for this study. The two Homalite-100 pieces of 229 mm × 190 mm × 9.5 mm are bonded together using a weak adhesive, Loctite-384. The quasi-static fracture toughness of the Loctite-384 adhesive when used to bond Homalite-100 sheets is 0.35 MPa-√m. This value of the interface fracture toughness is determined from three-point bending experiments in our laboratory. A small notch is made to wedge load the specimen. As mentioned above, such a large specimen is chosen to delay the arrival of the reflected waves from the edges of the specimen to the observation area as shown in Fig. 2. Of course, all reflected waves cannot be completely eliminated within a reasonable observation time from the field of view, in particular those reflected from the vertical surfaces in the vicinity of the notch. However, these disturbances are relatively weak and as the crack advances further away from these surfaces, their effect is reduced. As a result, we obtain substantially long records of constant crack speed, which ceases to be constant as reflected waves from distant boundaries interact with the crack tip.

A well known full-field experimental technique, dynamic photoelasticity, is employed. The experimental setup is shown in Fig. 2. It consists of a high power green laser (532 nm), a collimator, a set of circular polarizers, and a digital high-speed camera (manufactured by Cordin). The specimen is sandwiched between a set of circular polarizers and is illuminated using the expanded, collimated laser beam of diameter 135 mm approximately. Due to the birefringence property of Homalite-100, the set of circular polarizers generates photoelastic fringes. These fringes are also called isochromatics, and are basically contours of constant maximum shear stress. Photoelastic fringes associated with crack propagation are captured using a digital high-speed camera which has the capability of taking pictures at a framing rate as high as 100 million frames per second and with an exposure time as low as 10 ns. An inter-frame time of 30 μs is used to capture a crack propagation event along the weak planes. From these fringes a set of metrics associated with the crack propagation is identified. The details of these metrics are duly discussed in Section 4.

2.2. Design considerations for accurate loading conditions

In order to provide accurate loading conditions to the simulations, a loading setup is designed. The loading setup consists of a Hopkinson bar, a steel projectile and a steel wedge as shown in Fig. 3. The steel wedge is inserted into the notch of the specimen. The specimen with the wedge is held against the bar without any gap. A gas gun is used to impact the Hopkinson bar with a steel projectile. The impact generates a compressive pulse which passes through the bar and the wedge inserted into the specimen. This pulse then loads the notch faces of the specimen. A set of strain gage rosettes is attached to the sample at a distance of 4 mm from the notch faces. These rosettes record the strain values associated with the loading pulses. The strain pulses are later analyzed to obtain normal stress and shear stress pulses. These stress pulses are scaled for dispersion and applied as uniform normal and shear

Table 1
Material properties of Homalite-100 [3].

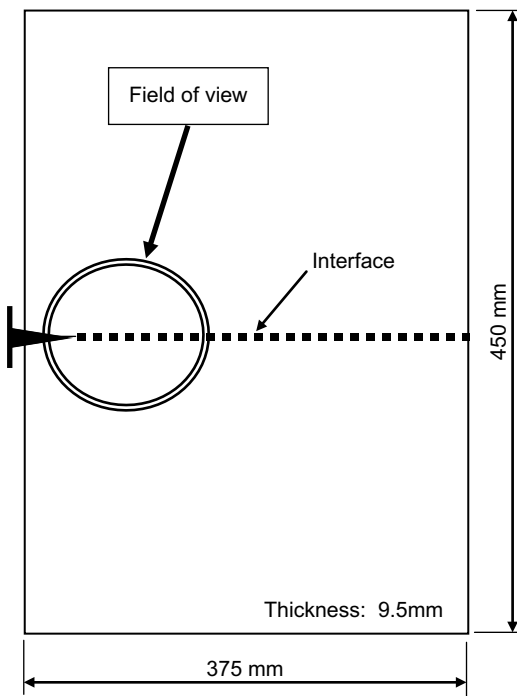| Property	Static ($\dot{\varepsilon} = 10^{-3}/s$)	Dynamic ($\dot{\varepsilon} = 10^3/s$)
Density (kg/m^3)	1230	1230
Young's modulus (GPa)	3.45	4.8
Dilatational wave speed (m/s)	1890	2119
Shear wave speed (m/s)	1080	1208
Rayleigh wave speed (m/s)	1010	1110
Poisson's ratio	0.35	0.35

Fig. 1. Specimen configuration with a field of view.

traction pulses. Details of the scaling of the original stress pulses are later discussed in Section 3. This setup is chosen to provide simple boundary conditions for the numerical simulations, and in particular all the edges of the specimen are stress free except the notch faces. Furthermore, the Hopkinson bar provides a well-controlled pulse, which can be measured with a strain gage mounted on the surface of the bar.

2.3. Design considerations for realistic cohesive zone laws

One of the major difficulties in applying cohesive zone models in engineering applications is the prescription of physically accurate cohesive zone laws. Viewed as an inverse problem, one can seek the cohesive law, i.e. separations and tractions near a crack tip, from the knowledge or measurements of the fields at an exterior boundary. It is well known that this type of inverse problem is severely ill-conditioned [21], so that a small amount of error in the input data for the inverse analysis can cause a catastrophic error in the final outcome. Therefore, systematic approaches are required in experimental measurements and data analysis to overcome the ill-conditioning. A framework developed by Hong and Kim [21] for the inverse analysis of the crack tip cohesive zone model is employed to
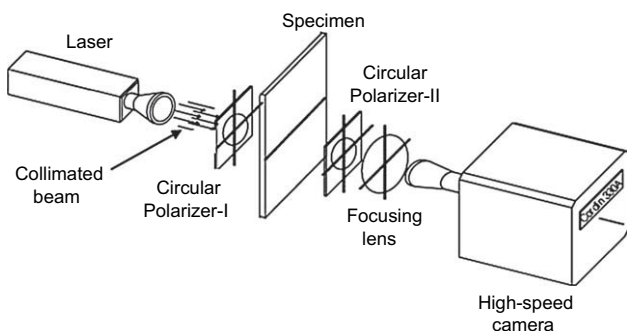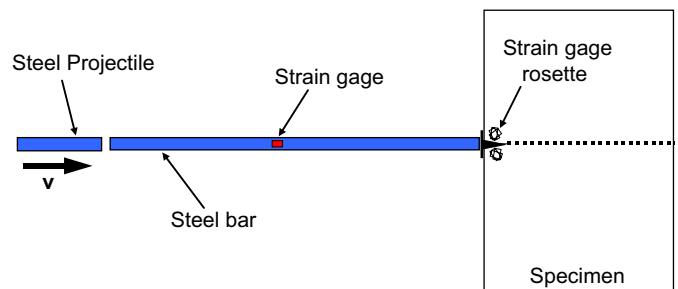

Fig. 2. Photoelastic experimental setup.

Fig. 3. Modified Hopkinson pressure setup for loading the specimen.

obtain a realistic cohesive zone law of the weak interface by following a series of experimental, numerical and analytical procedures.

First, an optical measurement technique called electronic speckle pattern interferometry (ESPI) was used to measure crack tip displacement fields surrounding a crack tip in a weak interface. The non-contacting and whole-field measurement capability of the ESPI can provide elastic deformation fields surrounding a fracture process zone that can be used as input data for the inverse analysis. The optical theory of ESPI and necessary image processing algorithms can be found elsewhere [22,23]. A laser speckle interferometer setup shown in Fig. 4 is constructed to measure the two-dimensional displacement around a crack tip during four-point bending fracture tests of an adhesive joint in Fig. 5. Optical phase measurements are conducted by using the spatial phase-shifting technique [24]. Also, horizontal and vertical displacement components are measured simultaneously and independently by separating the optical polarizations in each direction [25]. The optical measurement system is designed to provide far-field elastic deformation fields surrounding a fracture process zone with a high sensitivity and a high spatial resolution suitable for the inverse analysis of the crack tip cohesive zone problem. Then, a numerical noise reduction algorithm, called equilibrium smoothing method, is used to overcome the severe ill-conditioning in the inverse problem by removing experimental noises. The equilibrium smoothing method uses the governing field equation of isotropic linear elasticity in a domain as a constraint for a PDE constrained error minimization problem, in order to extract a smooth equilibrium field $u(x)$ that is closest to an experimentally measured displacement field $\tilde{u}(x)$ in the least-square sense. Also, an additional constraint of cubic spline smoothing is imposed along the boundary Γ of the domain Ω as given in Eqs. (1) and (2).

$$\text{Minimize } E[u(x); \alpha] = \frac{1}{2}\int_{\Omega} \left\| u - \tilde{u}\right\|^2 d\Omega + \frac{1}{2}\oint_{\Gamma} \alpha \left\|\frac{\partial^2 u}{\partial s^2}\right\|^2 d\Gamma \qquad (1)$$

$$\text{subjected to } \mu\nabla^2 u + (\lambda + \mu)\nabla(\nabla \bullet u) = 0 \text{ in } \Omega \qquad (2)$$

where λ and μ are Lame's constants, $x \in \Omega$ and $s \in \Gamma$. A finite element formulation of the equilibrium constraint and a finite-difference formulation of the boundary cubic spline term are incorporated into the global error minimization problem using the Lagrange multiplier method and the penalty function method, respectively. The equilibrium smoothing algorithm is applied to remove experimental noises in the crack tip displacement field measured by the speckle interferometer.

Finally, the analytical solution method [21] of the inverse problem is used to extract a cohesive zone law, i.e. a traction-separation law $t(\delta)$, from the smooth elastic far-field surrounding a crack tip fracture process zone. The solution method uses a general form of cohesive crack tip fields to obtain eigenfunction
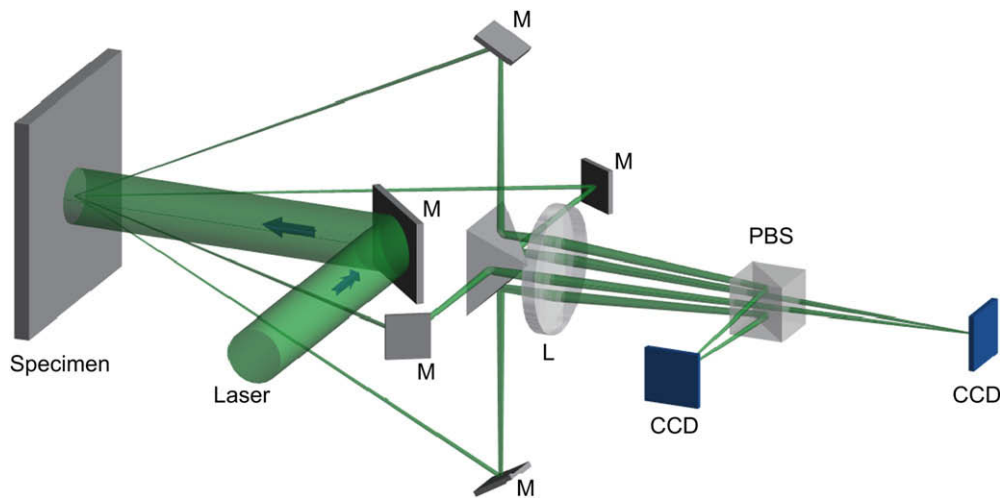
Fig. 4. Experimental setup to measure the crack tip displacement field using laser speckle interferometry.

expansions of the plane elastic field in a complex variable representation. In case of mode-I, the cohesive traction and the separation gradient within the cohesive zone ($-c \le x \le c$) are expressed in terms of two analytic functions, $F(x)$ and $G(x)$, from the general-form complex functions, as given in Eqs. (3) and (4).

$$t(x) = \sqrt{x + c}F(x) \tag{3}$$

$$b(x) = -\frac{d\delta(x)}{dx} = \frac{\kappa + 1}{2\mu}\sqrt{c - x}G(x) \tag{4}$$

where $\kappa = 3 - 4\nu$ for plane strain, $\kappa = (3 - \nu)/(1 + \nu)$ for plane stress and ν is Poisson's ratio. Using the Chebyshev polynomial of the second kind, Eqs. (3) and (4) can be represented with a set of cohesive crack tip eigenfunctions which is complete and orthogonal in the sense of the interaction J-integral at far-field as well as at the cohesive zone faces. The coefficients of the eigenfunctions in the J-orthogonal representation are extracted directly, using interaction J-integrals at far-field between the physical field and auxiliary probing fields. Then, the separation profile within the cohesive zone is found by integrating Eq. (4).

$$\delta(x) = \int_{x}^{c} b(\xi)d\xi \tag{5}$$

Thus, the parametric relationship between the traction and the separation within the cohesive zone provides a cohesive zone law. The path-independence of the interaction J-integral enables us to identify the cohesive zone variables, i.e. traction, separation gradient and separation, as well as a cohesive zone law uniquely from the far-field data.

3. Numerical design considerations

As mentioned above, an experimentalist may often employ large samples in order to make the experimental instrumentation simple and foolproof. However, this leads to large computer models, requiring substantial computer resources, in terms of both the number of processors, as well as, execution time.

Indeed, in dynamic fracture simulations the cohesive characteristic length needs to be resolved, by typically requiring this length to be spanned by five elements, in order to achieve results independent of the details of the finite element discretization. In particular, Loctite-384 has a characteristic length of $l_c = 1.267$ mm to be resolved. Consequently, if one decides to treat the original problem as two-dimensional (2D), the large disparity between the characteristic length of Loctite and the sample dimensions leads to computational models easily exceeding five million triangular elements. The size of the resulting finite element model is therefore significant. The complexity of the model may be reduced in a number of ways. Often, the approach of choice is adaptive mesh refinement (AMR) [26,27]. Implementations of AMR are notoriously complex and plagued by poor performance. Moreover, at present it is not entirely clear how to properly solve the AMR problem in the case of evolving mesh topology due to fracture. Here, we adopt an alternative route: employ uniform size meshes and utilize massively parallel computing environments. Uniform meshes offer an additional benefit of removing elastic wave dispersion characteristic of non-uniform meshes.
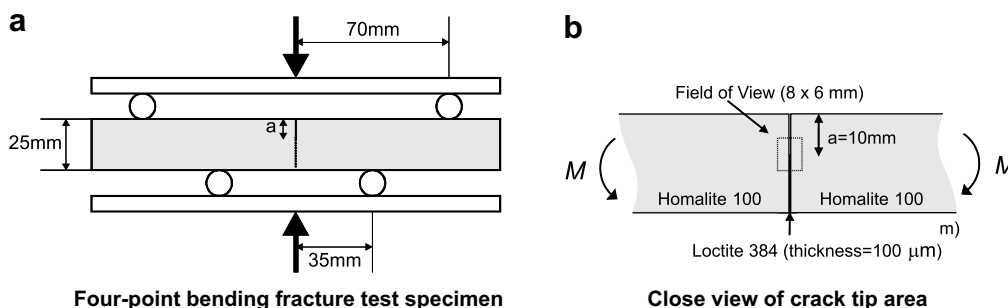

Four-point bending fracture test specimen

Close view of crack tip area

Fig. 5. Experimental setup for four-point bending fracture tests of adhesive joints. (a) Four-point bending fracture test specimen. (b) Close view of the crack tip area.
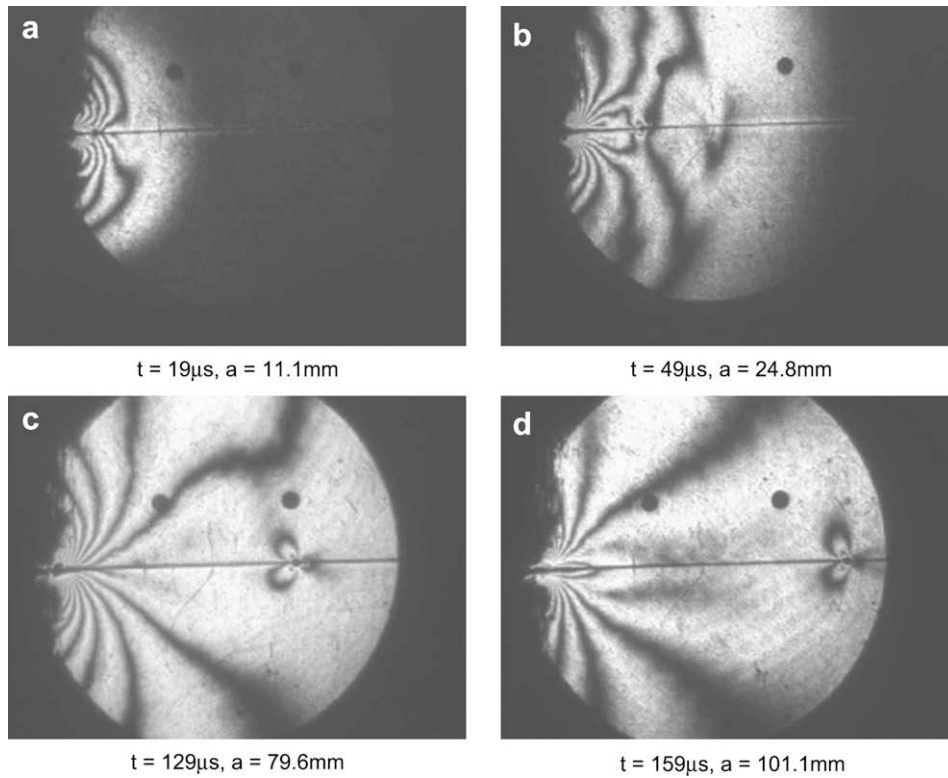
Fig. 6. Photoelastic isochromatic fringes associated with dynamic crack propagation along a weak interface (the circular dot is a scale of 6.25 mm). (a) $t = 19$ μs, $a = 11.1$ mm; (b) $t = 49$ μs, $a = 24.8$ mm; (c) $t = 129$ μs, $a = 79.6$ mm; (d) $t = 159$ μs, $a = 101.1$ mm.

For the purpose of reducing the computational complexity of the problem we have decided to treat the problems as two-dimensional (plane stress), in lieu of a fully three-dimensional approach. As observed by Pandolfi et al. [28], cracks propagating in thin plates do not exhibit a fully three-dimensional character, and the problems involving fracture of thin plates may be considered, with great accuracy, as two-dimensional. Therefore, we made sure that the thickness of the experimental sample is chosen so as to assure the validity of such simplifications.

Again, one of the major factors impacting the fidelity of computer simulations is the choice and accuracy of boundary conditions. Complex boundary conditions are not easily amenable to computer simulations, and may severely degrade the accuracy of computer predictions. Our experimental setup and instrumentation have been designed to eliminate any uncertainties regarding the boundary conditions. Therefore, we model the sample as traction free. The loading on the crack notch has been measured in the course of the experiment and the recorded data applied directly
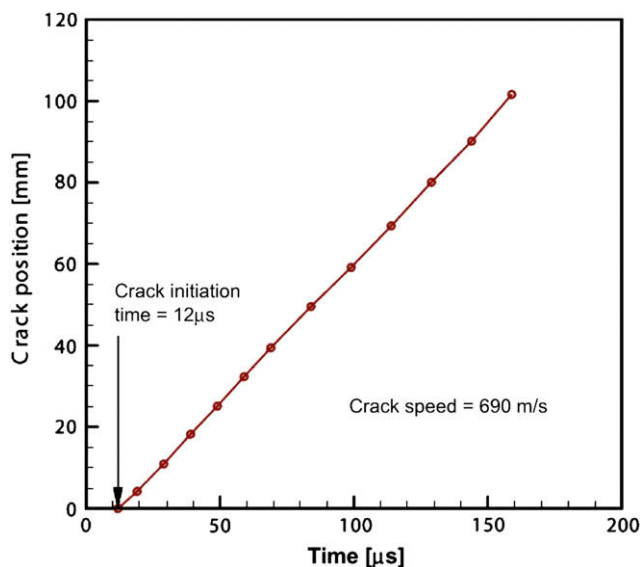

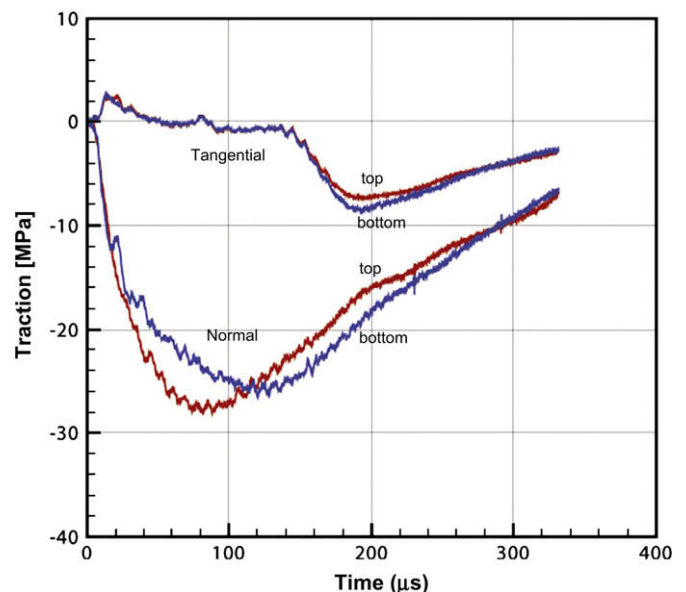**Fig. 7.** History of crack tip position along a weak plane.

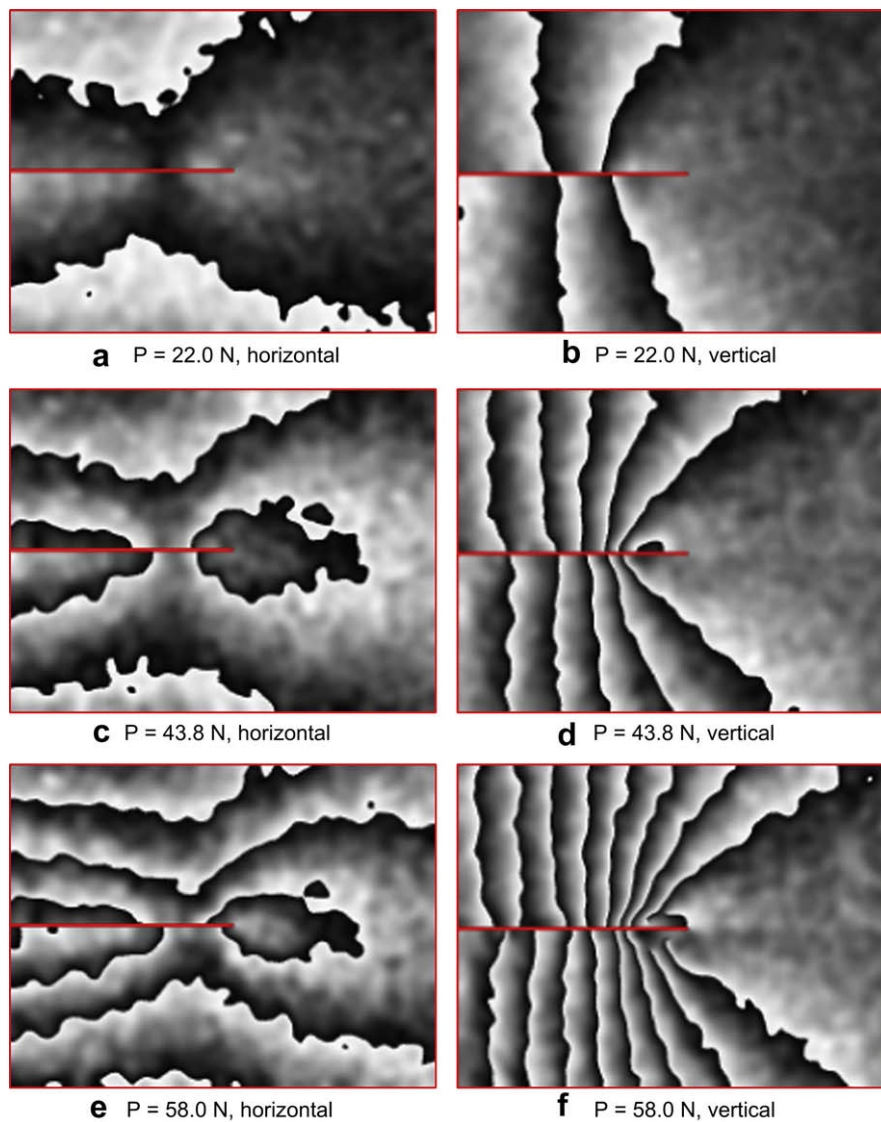**Fig. 8.** Normal and tangential traction pulses on the top and bottom notch faces.

Fig. 9. Cumulative wrapped displacement maps near the crack tip in both the horizontal and vertical directions as a function of load. (a) $P = 22.0$ N, horizontal. (b) $P = 22.0$ N, vertical. (c) $P = 43.8$ N, horizontal. (d) $P = 43.8$ N, vertical. (e) $P = 58.0$ N, horizontal. (f) $P = 58.0$ N, vertical.
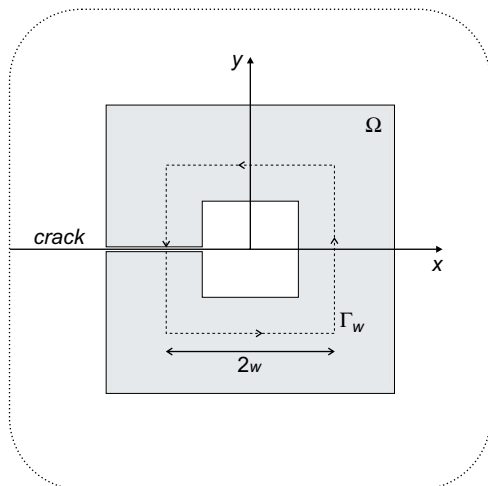

Fig. 10. Domain of equilibrium smoothing and J-integral contour.

into the simulation. This approach has proved very effective and allowed the boundary conditions to remain in strict agreement with their experimental counterparts. Here, the stress pulses on the notch faces provided by the experiments are directly imposed as Neumann boundary conditions on the finite element model.

Homalite-100 is a brittle polyester resin whose mechanical response is mildly rate sensitive [3]. Therefore in our simulations, we model the mechanical response of Homalite-100 as purely elastic. However, in an attempt to take the rate dependency into account we use the so-called 'dynamic' value of the Young's modulus as reported by Dally and Shukla [29]. This value is considered more representative of the mechanical response of Homalite-100 under the loading conditions in our experiments.

The process of initiation and growth of the crack along the interface is modeled with the formalism of Ortiz and Pandolfi [30]. In this approach, special elements, cohesive elements, are adaptively inserted in the finite element discretization of a body to simulate growing cracks. The cohesive element governs the separation of the crack flanks with a cohesive law. The versatility and predictive capability of the method have been demonstrated in numerous works [19,28,30–34]. The novelty of our approach is the use of the cohesive law as it is
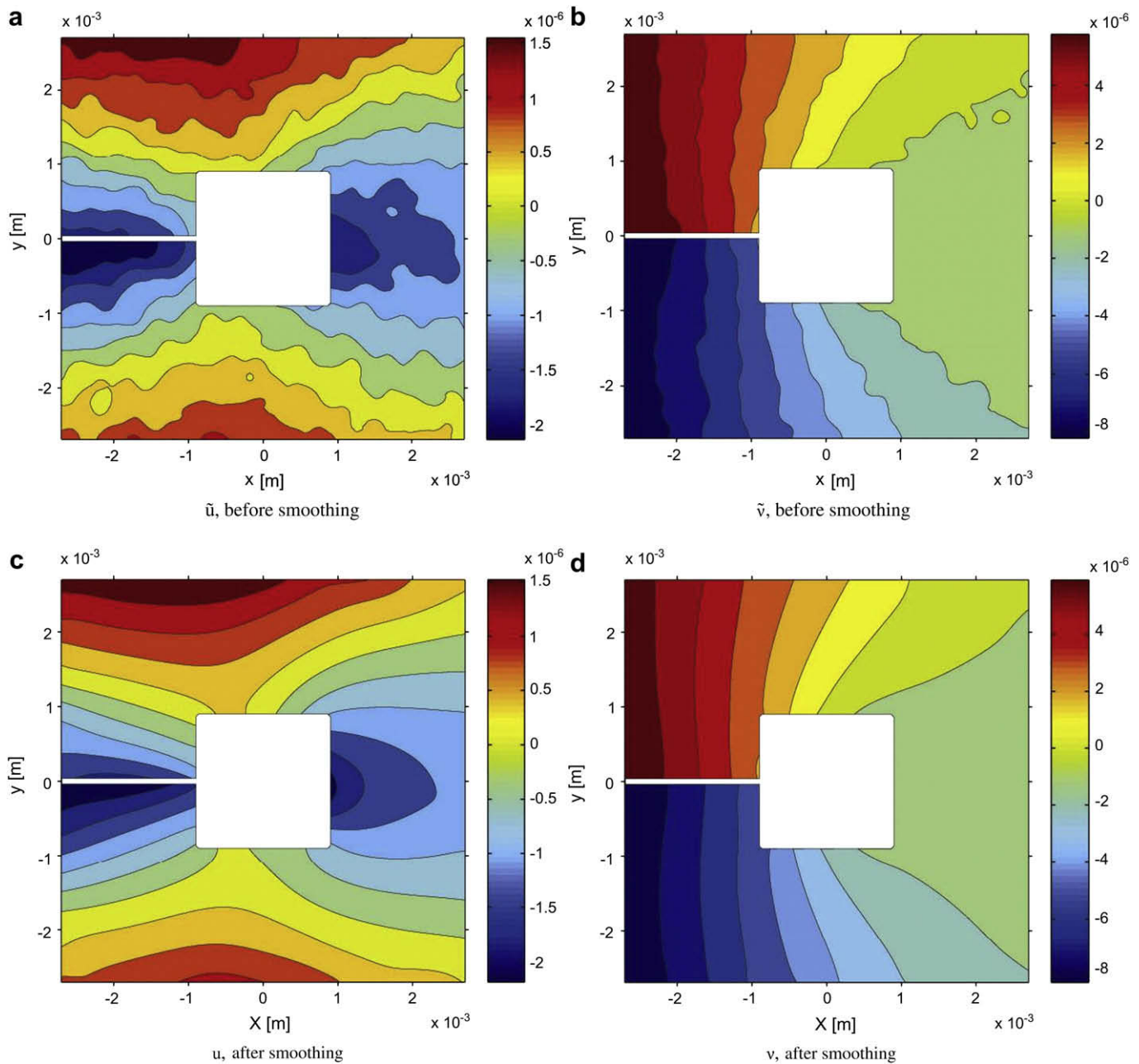
Fig. 11. Crack tip displacement fields before and after equilibrium smoothing. (a) $\tilde{u}$, before smoothing; (b) $\tilde{v}$, before smoothing; (c) u, after smoothing; (d) v, after smoothing.

obtained directly from the experiment, without the need for fitting or tuning. For numerical details, see Ref. [35].

The choice of metrics is at the heart of any V and V effort. These metrics should be fundamental to the underlying phenomena and be amenable to accurate experimental instrumentation. Moreover, they should be easily extractable from simulation results. In the problem of crack propagation along interfaces considered here, we have decided to employ the following set of validation metrics: crack initiation time, crack tip position and crack tip velocity. This choice satisfies the above requirements and gives the ability of a one-to-one direct comparison of the simulation results with the experimental data.

4. Results

The results obtained at various stages of this study are presented in the following sections. Some of the experimental results are later used as input to the simulations. Results of the final stage (metrics) of numerical simulations are compared with those of experiments to complete the validation process.

4.1. Results of the dynamic fracture experiments

The real-time records of photoelastic fringes associated with the propagation of a crack along a weak interface are shown in Fig. 6. The circular spot visible on each frame has a diameter of 6.25 mm, thus providing a scale to determine the crack tip velocity. Accurate crack tip positions for the propagating cracks can be inferred from the location of the center of small shadow spots corresponding to a traveling stress singularity as well as from the increased concentration of focused isochromatics at the crack tip. From these fringes, a set of metrics such as crack initiation time upon arrival of the loading pulse on the notch faces, crack tip position as a function of time, and crack tip velocity are identified and measured from the
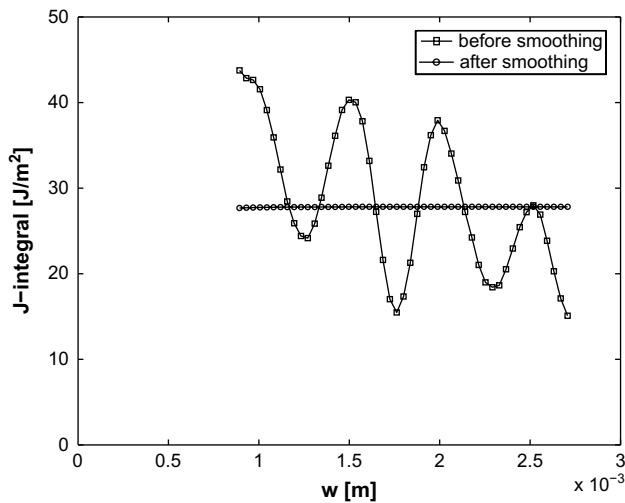
Fig. 12. J-integrals evaluated along various contours shown in Fig. 10.

experiments. Typical results of all these metrics for one of the experiments are shown in Fig. 7. As shown, the crack takes $t = 12 \, \mu s$ to initiate upon loading and propagates with an average constant velocity of 690 m/s.

4.2. Measurement of the boundary loading conditions

As mentioned in Section 2, the loading pulses provide one of the two primary inputs to the simulations. These loading pulses are measured from two sets of strain gage rosettes bonded near the top and bottom faces of the notch. The raw strain pulses recorded from the strain gage rosettes are analyzed for in-plane strain pulses using strain transformation equations. Using plane stress conditions, these in-plane strain pulses are used to determine the normal and shear stress pulses acting at the location of the strain gage rosettes. Typical normal and tangential traction pulses on the notch faces are shown in Fig. 8.

4.3. Results of the inverse problem

Displacement fields near a crack tip in an adhesive joint under the mode-I loading condition are incrementally measured by using the speckle interferometer and the four-point bending fracture test setup shown in Figs. 4 and 5 respectively. For each load increment value, optical phase measurements are conducted by using the spatial phase-shifting method. The obtained raw phase-change maps which correspond to wrapped displacement maps are low-pass filtered to remove high-frequency noise components. Then, the incremental phase-change maps are successively added to construct a cumulative wrapped displacement map in each loading
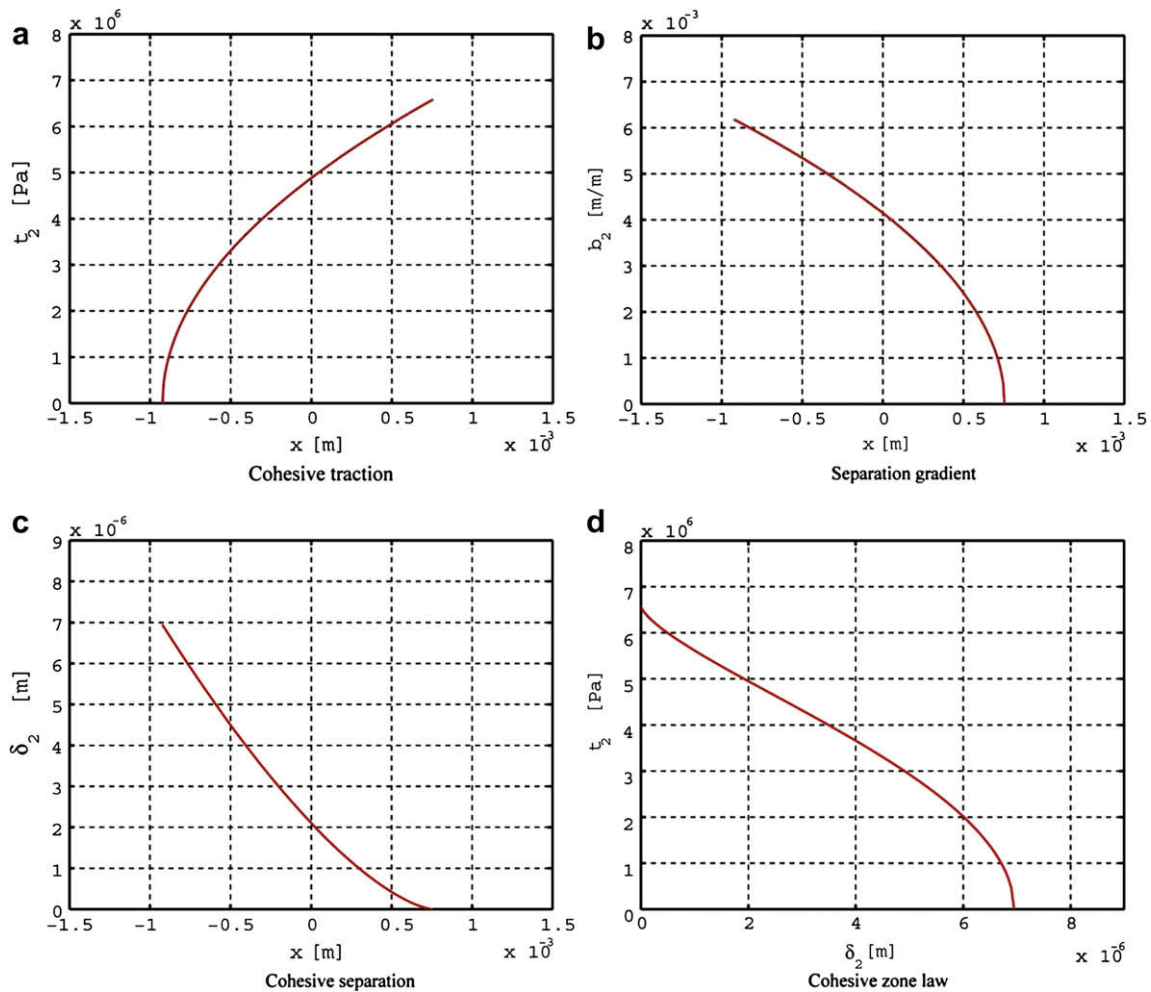

Fig. 13. Cohesive zone variables and cohesive zone law extracted from the crack tip deformation field. (a) Cohesive traction; (b) separation gradient; (c) cohesive separation; (d) cohesive zone law.
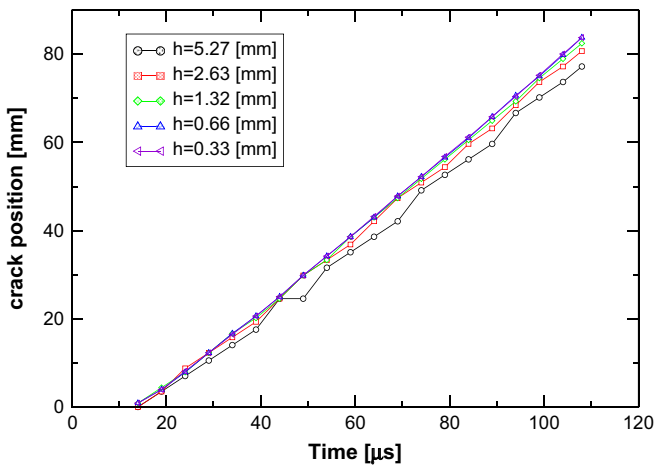
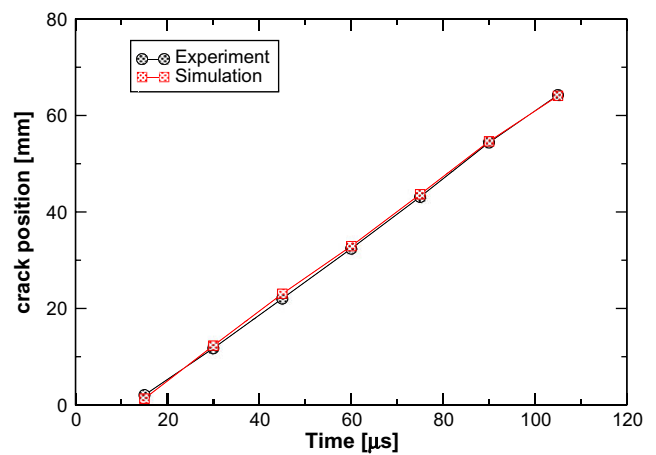**Fig. 14.** Simulated crack tip locations as a function of mesh sizes.

Fig. 16. Comparison of the experimental crack tip position (from experiment 2) with that of simulations.

step. Three sets of cumulative wrapped displacement fields in the horizontal and vertical directions are shown in Fig. 9. Each two-phase fringe represents a relative displacement of 1.20 μm according to the sensitivity calibrations in the field of view (8 mm × 6 mm). Symmetric two-phase fringe patterns with respect to the horizontal axis show that the rigid body rotation during the four-point bending test is well-suppressed. In order to use the obtained whole-field displacement data for the inverse analysis of the crack tip cohesive zone model, a further noise reduction is required to remove the remaining low-frequency noises.

The equilibrium smoothing algorithm is applied to remove the remaining experimental noises in the crack tip displacement fields. Among the cumulative displacement maps in Fig. 9, a set of wrapped displacement maps (e) and (f) is chosen as a crack tip displacement field at the onset of the crack propagation and unwrapped by removing the two-phase jumps. A square domain excluding a smaller square region near the crack tip in Fig. 10 is selected from the experimental field of view for equilibrium smoothing. After applying the equilibrium smoothing method to the set of unwrapped continuous displacement fields in Fig. 11 (a) and (b), a set of smooth equilibrium displacement fields is obtained and shown in Fig. 11 (c) and (d). The result shows that a significant amount of low-frequency fluctuations in the experimental data is removed successfully. Then, displacement gradient fields are calculated from the smooth equilibrium fields by numerical

differentiations. The obtained equilibrium deformation fields are used as input data for the characterization of the crack tip field using the conservation J-integral [36]. Fig. 12 shows the J-integral values evaluated along various contours shown in Fig. 10 before and after equilibrium smoothing. The J-integral value evaluated from the smooth deformation field is 27.5 J/m^2 and shows a good path-independence.

The analytical solution method of the inverse problem of the crack tip cohesive zone model is used to extract a cohesive zone law of the weak interface from the smooth equilibrium deformation fields. Fig. 13 shows profiles of the extracted cohesive zone variables within the cohesive zone, namely (a) cohesive traction, (b) separation gradient and (c) cohesive separation, as well as (d) the cohesive zone law extracted from the smooth equilibrium deformation fields near the fracture process zone. The cohesive zone law in Fig. 13 (d) is parametrically constructed from the cohesive traction and the cohesive separation within the cohesive zone. As the order of the polynomial series expansions of (3) and (4) increases, the extracted cohesive zone variables showed erratic behaviors due to the ill-conditioning of the inverse problem. Thus, the extracted results are obtained by using only the first terms in the expressions. Therefore, the extracted cohesive zone variables must be considered as approximations of the actual cohesive zone variables up to the cutoff polynomial order. The extracted cohesive zone law must be considered as an approximation which can be represented with
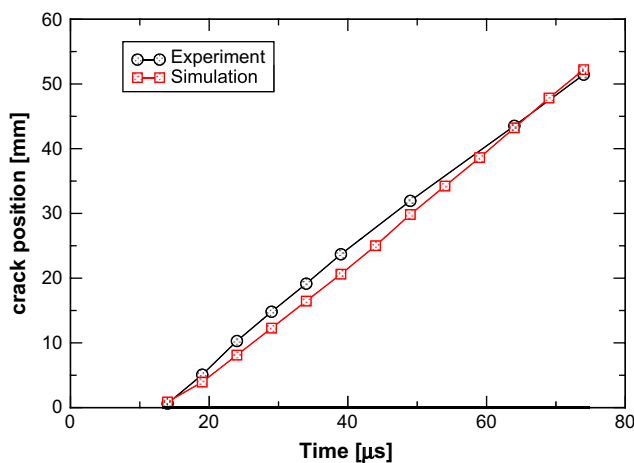

Fig. 15. Comparison of the experimental crack tip position (from experiment 1) with that of simulations.
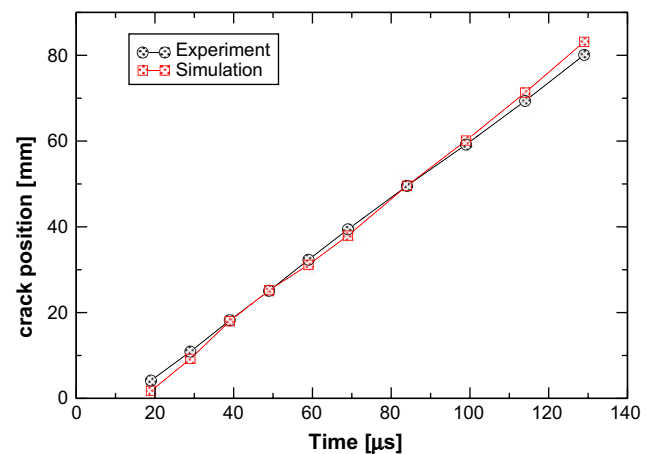

Fig. 17. Comparison of the experimental crack tip position (from experiment 3) with that of simulations.

Table 2
Comparison of the experimental crack tip velocity with that of simulations.

Experiment no.	Crack tip velocity (m/s)		Relative error (%)
	Experiment	Simulation	
1	844	870	3.1
2	697	698	0.1
3	688	729	6.0

two independent parameters. The area under the curve in Fig. 13 (d) represents the cohesive fracture energy of 26.8 J/m^2 and agrees well with the far-field J-integral value of 27.5 J/m^2 in Fig. 12. The extracted cohesive zone laws are provided as one of the input data for large-scale simulations of dynamic fracture along the weak interface.

4.4. Results of numerical simulations

The initial goal of our simulation effort has been to establish the convergence properties of the numerical model. As we mentioned before, we resort to uniform discretizations and utilize massively parallel computing environments in order to cope with the computational complexity of the problem. We begin with a coarse triangular mesh characterized by an element size of $h = 5.27$ mm, or equivalently $h/l_c = 4.16$, where l_c is the characteristic cohesive length. Finer meshes are obtained from the coarse mesh by recursive uniform subdivision. We terminate the subdivision process once the element size reaches $h = 0.33$ mm, or $h/l_c = 0.26$ (approximately four elements per characteristic cohesive length). Fig. 14 shows the simulated location of the crack tip for different mesh sizes. As expected, the results depend strongly on the element size h. However, as h approaches l_c, the characteristic cohesive length, the numerical predictions converge, with the curves corresponding to $h = 0.66$ mm and $h = 0.33$ mm being virtually indistinguishable.

We have carried out a validation study on a set of three independent experimental realizations (experiment 1, experiment 2 and experiment 3). The sole difference between these realizations is in the loading at the notch surfaces, with all other aspects being identical. Figs. 15–17 display the crack tip position vs. time for experiment 1–3. We show both the experimental data and simulation predictions. We have used these curves to compute the mean crack velocity as the slope of the linear regression fit to the data.
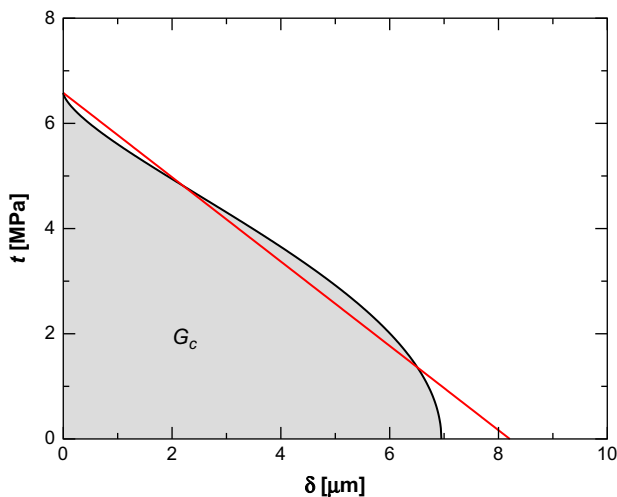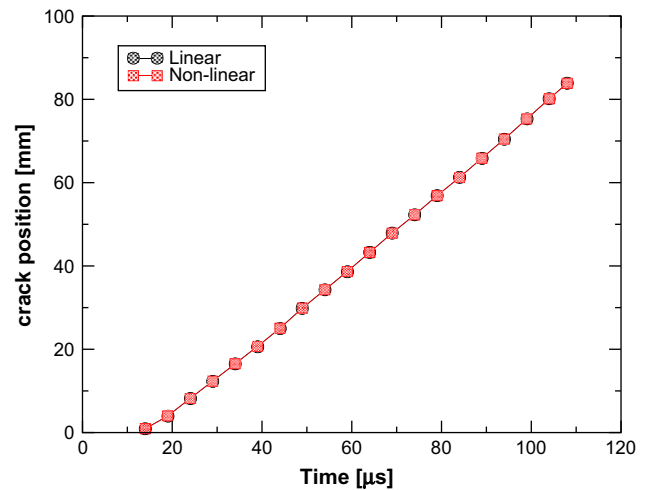
Fig. 19. Crack tip position vs. time for experiment 1 with two different cohesive zone laws.

These results are presented in Table 2, along with the relative error of the numerical predictions with respect to those obtained from the experimental data. In addition to the crack tip position and the crack mean velocity we have compared the crack initiation time. The experimental data have been ostensibly uniform with respect to the crack initiation time; all three experiments recorded the onset of crack growth at 13 μs with 1 μs granularity. Applying the same granularity to the numerical results we obtained exactly the same crack initiation time, with simulations of all three experiments giving the value of 13 μs.

In addition to the systematic validation of the cohesive finite element models, we have investigated the sensitivity of the numerical predictions to the functional form of the cohesive law. To this end, we have replaced the experimentally extracted cohesive law in Fig. 13 (d) with the linear decay envelope as shown in Fig. 18. We fit the linear cohesive law assuming that the critical strain energy release rate G_c (corresponding to the area under the traction-separation curve) and the critical traction t_c in the linear model match their experimental counterparts. The crack tip position vs. time corresponding to both of these cohesive laws is plotted in Fig. 19. The results appear seemingly insensitive to the functional form of the cohesive law.

5. Conclusions

Well-controlled experiments are conducted to provide valid boundary conditions and accurate mode-I cohesive zone laws as inputs for conducting and validating large-scale dynamic fracture simulations along weak planes. The experimental setup provides high resolution data on metrics preselected for the validation of the simulations. These metrics are representative of the key phenomenon under study, interfacial dynamic crack propagation. The simulations are performed using cohesive elements, which are adaptively inserted in the finite element discretization of the body to simulate growing cracks. The cohesive elements govern the separation of the crack flanks with the experimentally obtained cohesive zone law. Numerical results of the crack initiation time and crack tip position as a function of time are compared with those experiments. The results show a good comparison and strong consistency with respect to the crack initiation time and average crack tip velocity. The consistency is verified by comparing three different simulations with the corresponding experiments. It was also confirmed that the detailed shape of the non-linear cohesive zone law has no significant influence on the numerical results.

Fig. 18. Experimentally obtained cohesive zone law and the corresponding linear cohesive zone law.

Acknowledgements

References

[1] Broberg KB. Cracks and fracture. San Diego: Academic Press; 1999. p. 328–539.
[2] Freund LB. Dynamic fracture mechanics. Cambridge: Cambridge University Press; 2002. p. 296–365.
[3] Rosakis AJ. Intersonic shear cracks and fault ruptures. Adv Phys 2002;51(4):1189–257.
[4] Bradley WB, Kobayashi AS. Fracture dynamics – a photoelastic investigation. Eng Fract Mech 1971;3:317–32.
[5] Kobayashi AS, Mali S. Dynamic fracture toughness of Homalite-100. Exp Mech 1978;18:11–8.
[6] Dally JW. Dynamic photoelastic studies of fracture. Exp Mech 1979;19:349–67.
[7] Rosakis AJ. Analysis of the optical method of caustics for dynamic crack propagation. Eng Fract Mech 1980;13:331–47.
[8] Rossamanith HP, Shukla A. Dynamic photoelastic investigation of interaction of stress waves with running cracks. Exp Mech 1981;21:415–22.
[9] Washabaugh PG, Knauss WG. A reconciliation of dynamic crack velocity and Rayleigh wave speed in isotropic brittle solids. Int J Fract 1994;65:97–114.
[10] Hao S, Liu WK, Klein PA, Rosakis AJ. Modeling and simulation of intersonic crack growth. Int J Solids Struct 2004;41(7):1773–99.
[11] Scheider I, Schödel M, Brocks W, Schönfeld W. Crack propagation analyses with CTOA and cohesive model: comparison and experimental validation. Eng Fract Mech 2006;73:252–63.
[12] Haj-Ali R, El-Hajjar R, Muliana A. Cohesive fracture modeling of crack growth in thick-section composites. Eng Fract Mech 2006;73:2192–209.
[13] Rosakis AJ, Samudrala O, Coker D. Cracks faster than the shear wave speed. Science 1999;284(5418):1337–40.
[14] Kandula SSV, Abanto-Bueno J, Geubelle PH, Lambros J. Cohesive modeling of dynamic fracture in functionally graded materials. Int J Fract 2005;132:275–96.
[15] Parameswaran V, Shukla A. Dynamic fracture of a functionally gradient material having discrete property variation. J Mater Sci 1998;33:3303–11.
[16] Evora V, Jain N, Shukla A. Static and dynamic fracture toughness and crack propagation in nanocomposites. In: Proceedings of the society of experimental mechanics annual conference, Costa Mesa, CA; 2004.
[17] Mohammed L, Liechti KM. Cohesive zone modeling of crack nucleation at biomaterial corners. J Mech Phys Solids 2000;48(4):735–64.
[18] Needleman A. A continuum model for void nucleation by inclusion debonding. J Appl Mech 1987;54(3):525–31.
[19] Needleman A. An analysis of decohesion along an imperfect interface. Int J Fract 1990;42(1):21–40.
[20] Bjerke TW, Lambros J. Theoretical development and experimental validation of a thermally dissipative cohesive zone model for dynamic fracture of amorphous polymers. J Mech Phys Solids 2003;51(6):1147–70.
[21] Hong S, Kim KS. Extraction of cohesive-zone laws from elastic far-fields of a cohesive crack tip: a field projection method. J Mech Phys Solids 2003;51(7):1267–86.
[22] Jones R, Wykes C. Holographic and speckle interferometry: a discussion of the theory, practice and application of the techniques. Cambridge, New York: Cambridge University Press; 1983. p. 165–196.
[23] Rastogi PK. Digital speckle pattern interferometry and related techniques. Chichester, England: Wiley; 2001. p. 59–140.
[24] Sirohi RS, Burke J, Helmers H, Hinsch KD. Spatial phase shifting for pure in-plane displacement and displacement-derivative measurements in electronic speckle pattern interferometry (ESPI). Appl Opt 1997;36(23):5787–91.
[25] Moore AJ, Lucas M, Tyrer JR. An electronic speckle pattern interferometer for two-dimensional strain measurement. Meas Sci Technol 1996;7(12):1740–7.
[26] Jones M, Plassmann PE. Adaptive refinement of unstructured finite element meshes. Finite Elem Anal Des 1997;25(1-2):41–60.
[27] Bern MW, Plassmann PE. Mesh generation. In: Sack J, Urrutia E, editors. Handbook of computational geometry. North Holland: Elsevier Scientific; 2000. p. 291–332.
[28] Pandolfi A, Guduru P, Ortiz M, Rosakis AJ. Three dimensional cohesive-element analysis of dynamic fracture in C300 steel. Int J Solids Struct 2000;37(27):3733–60.
[29] Dally JW, Shukla A. Energy loss in Homalite-100 during crack propagation and arrest. Eng Fract Mech 1980;13(4):807–17.
[30] Ortiz M, Pandolfi A. Finite-deformation irreversible cohesive elements for three-dimensional crack-propagation analysis. Int J Numer Methods Eng 1999;44(9):1267–82.
[31] Xu XP, Needleman A. Void nucleation of fast crack-growth in brittle solids. J Mech Phys Solids 1994;42(9):1397–434.
[32] Camacho GT, Ortiz M. Computational modeling of impact damage in brittle materials. Int J Solids Struct 1996;33(20-22):2899–938.
[33] Ruiz G, Ortiz M, Pandolfi A. Three-dimensional finite-element simulation of the dynamic Brazilian tests on concrete cylinders. Int J Numer Methods Eng 2000;48(7):963–94.
[34] Nguyen O, Repetto EA, Ortiz M, Radovitzky RA. A cohesive model of fatigue crack growth. Int J Fract 2001;110(4):351–69.
[35] Arias I, Knap J, Chalivendra VB, Hong S, Ortiz M, Rosakis AJ. Numerical modeling and experimental validation of dynamic fracture events along weak planes. Comput Methods Appl Mech Eng 2007;196:3833–40.
[36] Rice J. A path independent integral and the approximate analysis of strain concentration by notches and cracks. J Appl Mech 1968;35:379–86.